Nat Struct Mol Biol. Author manuscript; available in PMC 2015 December 01.

Published in final edited form as:
Nat Struct Mol Biol. 2015 June ; 22(6): 458–465. doi:10.1038/nsmb.3016.

Repulsive Guidance Molecule is a structural bridge between Neogenin and Bone Morphogenetic Protein

Eleanor G. Healey[1], **Benjamin Bishop**[1], **Jonathan Elegheert**[1], **Christian H. Bell**[1,#], **Sergi Padilla-Parra**[1,2], and **Christian Siebold**[1]

[1]Division of Structural Biology, Wellcome Trust Centre for Human Genetics, University of Oxford, Oxford, United Kingdom

[2]Cellular Imaging Core, Wellcome Trust Centre for Human Genetics, University of Oxford, Oxford, United Kingdom

Abstract

Repulsive guidance molecules (RGMs) control crucial processes spanning cell motility, adhesion, immune cell regulation and systemic iron metabolism. RGMs signal via two fundamental signaling cascades: the Neogenin (NEO1) and the Bone Morphogenetic Protein (BMP) pathways. Here, we report crystal structures of the N-terminal domains of all human RGM family members in complex with the BMP ligand BMP2, revealing a novel protein fold and a conserved BMP-binding mode. Our structural and functional data suggest a pH-linked mechanism for RGM-activated BMP signaling and offer a rationale for RGM mutations causing juvenile hemochromatosis. We also determined the ternary BMP2–RGM–NEO1 complex crystal structure, which combined with solution scattering and live-cell super-resolution fluorescence microscopy, indicates BMP-induced clustering of the RGM–NEO1 complex. Our results show how RGM acts as the central hub linking BMP and NEO1 and physically connecting these fundamental signaling pathways.

Correspondence should be addressed to C.S. (christian@strubi.ox.ac.uk).
[#]Current address: Roche Diagnostics GmbH, Penzberg, Germany.

AUTHOR CONTRIBUTIONS

C.S. designed and supervised the project. E.G.H. and C.H.B. cloned all RGM, NEO1 and BMP constructs. E.G.H., B.B. and C.H.B. performed protein expression and purification and E.G.H. crystallized the proteins. E.G.H. and C.S. collected the data and solved and refined the crystal structures. E.G.H. and B.B. carried out SPR and luciferase experiments and E.G.H performed the MALS experiments. SAXS data was collected by J.E. and E.G.H. and J.E. conducted all subsequent SAXS data processing. E.G.H, B.B. and S.P-P. collected the imaging data and S.P-P. completed the dSTORM data processing. C.S. and E.G.H. wrote the paper, and all authors discussed the results and commented on the paper.

Accession codes.

Atomic coordinates and structure factors for the $RGMA_{ND}$–BMP2, $RGMB_{ND}$–BMP2 Form 1, $RGMB_{ND}$–BMP2 Form 2, $RGMC_{ND}$–BMP2 and eRGMB–BMP2–$NEO1_{FN56}$ crystal structures have been deposited in the Protein Data Bank (PDB) under accession numbers 4UHY, 4UHZ, 4UI0, 4UI1, and 4UI2.

COMPETING FINANCIAL INTERESTS

The authors declare no competing financial interests.

Europe PMC Funders Author Manuscripts

INTRODUCTION

Repulsive guidance molecules (RGMs) are glycophosphatidylinositol (GPI)-anchored glycoproteins. There are three mammalian family members, RGMA, RGMB (also known as DRAGON) and RGMC (also known as hemojuvelin, HFE2). RGM dysfunction is linked to regenerative failure[1], inflammation[2], multiple sclerosis[3], cancer[4] and blood diseases[5]. RGMs were initially discovered as a repulsive axon guidance cue[6], where they signal by binding to the cell surface receptor neogenin (NEO1)[7,8], which belongs to the immunoglobulin superfamily and shares homology with the receptor deleted in colorectal cancer (DCC). We previously showed that this process is triggered by two RGM molecules that act as a molecular staple, bringing together the juxtamembrane regions of two NEO1 receptors, thus resulting in downstream signaling and actin cytoskeleton rearrangements[9]. All RGM family members have also been identified as co-receptors for the BMP morphogen pathway[10-12], a process that was previously suggested to be modulated by NEO1[13,14].

BMPs comprise the largest subgroup of the Transforming Growth Factor β (TGFβ) superfamily and are key players in embryonic development and in the adult[15]. The active BMP signaling complex consists of the BMP ligand, a constitutive disulfide-linked dimer, concomitantly binding to the BMP type I and type II receptors. Four different BMP type I receptors (ALK1, ACVR1, BMPR1A and BMPR1B) and three BMP type II receptors (ACVR2A, ACVR2B and BMPR2) have been identified[16,17]. Ligand binding triggers intracellular phosphorylation and activation of the type I receptor kinase domain by the constitutively active type II receptor kinase[18]. Subsequent downstream signaling occurs either via the SMAD signaling cascade[19], or via less well characterized alternative pathways[20]. The cellular localization and the site of action of TGFβ and BMP receptors are still under debate and endocytosis has been shown to be important for TGFβ and BMP signaling[21]. BMP receptors (type I and II) undergo constitutive clathrin-mediated endocytosis even in the absence of the BMP ligand, resulting in a potentiation of SMAD-dependent BMP signaling upon BMP ligand exposure[22]. Moreover, BMPR2 is also internalized through caveolae and the balance between caveola- and clathrin-mediated endocytosis is suggested to modulate the patterns of gene transcription initiated by BMP signaling[22,23]. In addition to receptor endocytosis, the BMP ligand itself can be readily internalized[24] and components of the SMAD signaling cascade are recruited to endosomal structures for activation[25].

Multiple effector proteins act to regulate and fine tune spatio-temporal levels of BMP signaling at the membrane[26]. These include soluble secreted antagonists (such as Noggin, Chordin and the DAN or Cerberus protein family), transmembrane proteins (e.g. BAMBI and Endoglin) and the membrane-attached RGM family. RGMs are important co-receptors and activators for BMP signaling. RGMA and RGMB were initially identified in cellular BMP reporter assays[11,12]. In addition, RGMB negatively regulates IL-6 expression in macrophages in a BMP ligand-dependent manner[27]. RGMC has been shown to enhance BMP signaling in liver cells to upregulate hepcidin expression and thereby control blood iron levels[10], and mutations in RGMC cause the blood iron overload disease juvenile hemochromatosis (JHH)[5,28,29], a pathology resulting from impaired BMP signaling[10,30]. All RGMs can bind directly to BMPs with nanomolar affinities[31,32], however the molecular

mechanism by which RGMs activate BMP signaling and the role of NEO1 in these processes remains unclear.

To elucidate the molecular mechanism of RGM-activated BMP signaling we solved crystal structures of BMP2 in complex with all human RGMs. Together with biophysical and cellular experiments, these structures suggest a mechanism for RGM-mediated activation of BMP signaling that is potentially linked to subcellular localization and offer a molecular rationale for JHH caused by RGM mutations. To address the role of NEO1 in these processes we determined the crystal structure of a ternary BMP–NEO1–RGM complex, which combined with X-ray solution scattering and quantitative super-resolution microscopic clustering analyses, provides direct evidence of a physical link between the NEO1 and BMP pathways bridged by RGMs, thus putting forward an important new mechanism for cellular signaling.

RESULTS

The structure of the BMP-RGM complex

We solved the crystal structure of human BMP2 in complex with the N-terminal domain of human RGMC ($RGMC_{ND}$) to 2.35 Å resolution (Fig. 1, Supplementary Fig. 1, 2 and Table 1). In the complex, two molecules of RGMC bind to one disulfide-linked BMP2 dimer (Fig. 1a-c and Supplementary Fig. 2). The RGMC molecules are related by a non-crystallographic pseudo-twofold axis and have an r.m.s.d. of 0.73 Å for 66 equivalent Cα positions. $RGMC_{ND}$ adopts a novel fold composed of a triple helix bundle stabilized by three disulfide bonds (Fig. 1b, c, d and Supplementary Fig. 3a, b). $RGMC_{ND}$ binds to the “finger” region of BMP2, interacting with both BMP2 molecules (Fig. 1d-f). The RGM interface on BMP2 is highly conserved in all vertebrate BMP2, BMP4, BMP6 and BMP7 family members (Fig. 1e and Supplementary Fig. 1). RGMC contacts both molecules of the disulfide-linked BMP2 dimer (total buried surface area of 1690 $Å^2$), an interaction that displays mixed electrostatics (6 hydrogen bonds, and 105 non-bonded contacts, Fig. 1f).

RGMA and RGMC contain a conserved RGD motif (traditionally known to be important in integrin-fibronectin mediated adhesion[33,34]). This motif, containing RGMC residues R98, G99 and D100, located in a loop region between helices α2 and α3, forms a major interaction site with BMP2 (Fig. 2a, b, residues highlighted by asterisks). Specifically, RGMC residues R98 and G99 provide several hydrogen bonds and non-bonded contacts (Fig. 2b), thereby positioning RGMC–H104 to allow the formation of a π-stacking interaction with BMP2–W313 (Fig. 2c). This arrangement is further stabilized by a T-shaped, orthogonal π-stacking between BMP2 residues W313 and W310. Intriguingly, mutations of RGMC residues G99 (of the proposed RGD motif) and L101, located in the center of the BMP-binding interface, cause the severe iron overload disease JHH[5,28,35] (Fig 2b).

To validate our structural data, we carried out surface plasmon resonance (SPR) equilibrium binding experiments (Fig. 2d–g). Our SPR analysis revealed a level of non-specific interaction between RGMs and BMP2, an effect that was markedly decreased for the N-terminal domain RGM constructs. Both the full length RGM ectodomain constructs

(eRGMA, eRGMB, eRGMC) and the RGM N-terminal domain constructs ($RGMA_{ND}$, $RGMB_{ND}$, $RGMC_{ND}$) bound to BMP2 with nanomolar affinities (the tightest being $RGMB_{ND}$ (K_d 88 nM)) demonstrating that the RGM N-terminal domain is sufficient for interaction with BMP2 (Fig. 2d, e and Supplementary Fig. 4). In addition, mutation of RGMC–H104 to alanine impaired binding to BMP2 (From K_d 124 nM to K_d 280 nM) (Fig. 2e, Supplementary Fig. 4f, g). This confirmed that the conserved RGMC–H104 is important for efficient complex formation through a π-stacking interaction with BMP2–W313; a similar behavior was observed for the RGMB–H106R mutation (Supplementary Fig. 4l).

We also solved the crystal structures of BMP2 in complex with the N-terminal domains of human RGMA and RGMB ($RGMA_{ND}$ and $RGMB_{ND}$, respectively) (Fig. 3, Table 1). A structural superposition revealed that the overall complex architecture (Fig. 3a) and BMP2-binding mode (Fig. 3b-e) is highly conserved across all RGM family members and in all species (Supplementary Fig. 1), demonstrating a common mode for the BMP–RGM interaction.

The RGMC–BMP2 structure offers a rationale for JHH mutations

JHH is an autosomal-recessive iron overload disorder that results in cardiomyopathy and diabetes. JHH is caused by a deficiency in the levels of hepcidin, whereas an excess of hepcidin is linked to anemia of inflammation[36,37]. RGMC-activated BMP signaling is crucial for upregulation of hepcidin expression and control of serum iron level, and mutations in RGMC are the major cause of JHH[5,10]. Most of these mutations are located in the C-terminal domain of RGMC, the region responsible for NEO1 binding (Fig. 1a)[9]. These mutations impair protein secretion in mammalian cells, whereas mutations located in the RGMC N-terminal domain do not affect secretion[9,38]. Here, we show that two of these, RGMC–G99R and –L101P are located in the interface with BMP2 and reduce the affinity of the RGMC–BMP2 interaction (K_d 910 nM, 1.5 μM respectively) (Fig. 2f, g and Supplementary Fig. 4h, i). This not only validates the interface observed in our RGM_{ND}–BMP2 structures, but also suggests that disruption of the BMP–RGMC interaction is the molecular mechanism for JHH disease pathology. Taken together, our analysis may provide a basis for the structure-guided design of novel therapeutics for the treatment of iron related disorders such as hemochromatosis and anemia of inflammation.

RGM competes with the BMP type I receptor for BMP2-binding

Crystal structures of BMP ligands with their respective receptor ectodomains have revealed a common mode of binding in which two BMP type I and II receptor molecules bind independently to a BMP dimer in a symmetric arrangement[39-41]. In our RGM–BMP2 structures, RGM_{ND} unexpectedly shares an overlapping BMP2-binding interface with the ectodomain of the BMP type I receptor BMPR1A (eBMPR1A; Fig. 4a, b), however the BMP type II receptor (eBMPR2, eACVR2A) binding site does not overlap (Fig. 4a). To confirm this observation drawn from our structural analysis, we carried out a series of SPR experiments. The secreted ectodomain of BMPR1A (eBMPR1A) bound to BMP2 with a K_d of 280±10 nM (Fig. 4c), in agreement with previous studies[42] and comparable to the RGMB–BMP2 interaction (Supplementary Fig. 4b, e). In this experimental setup, we did not detect specific binding between eRGMB and BMP receptor ectodomain constructs

(eBMPR1A, eBMPR2, eACVR2A) (Supplementary Fig. 4p-r), in contrast to previously reported pull-down experiments with full-length BMP receptors[11]. Next, we tested the ability of eBMPR1A to compete with eRGMB for BMP2 binding (Fig. 4d). We observed that a 1.7 times molar excess of eBMPR1A was required to displace eRGMB in solution suggesting that eRGMB effectively competes with eBMPR1A for BMP binding as expected from our structural data.

The RGM–BMP2 interaction is pH-dependent

Although the structures of eBMPR1A and RGM_{ND} are distinct, both share a common helix located at the interface with BMP2 (Fig. 4a, b), which is part of the BMPR1A epitope previously identified to be crucial for BMP2 interaction[43]. In this key helix, RGMB–H106 (corresponding to RGMC–H104) occupies the equivalent position to BMPR1A–F108. Both residues are involved in π-stacking interactions with BMP2 residues W310 and W313 (Fig. 3c, 4b and 2d, e). With the hypothesis that the protonation state of RGMB–H106 might affect the BMP2–W313 π-stacking, we performed multi-angle light scattering (MALS) measurements of both BMP2–$RGMB_{ND}$ and BMP2–eBMPR1A complexes at different pH values (Fig. 4e, f). For BMP2–$RGMB_{ND}$, we observed a major species at neutral pH with a molecular weight corresponding to the 2:2 BMP2–RGM_{ND} complex, whereas at pH 6.5 or lower, dissociation of the complex occurred (Fig. 4e). Our data showed that the BMP2–$RGMB_{ND}$ interaction is pH dependent, whereas the binary 2:2 BMP2–eBMPR1A complex is not (Fig. 4f).

RGMB and BMPR1A differentially alter BMP signaling

How does RGM activate BMP signaling when it competes with the canonical BMP binding mode for BMP type I receptors? In order to answer this, we conducted a BMP-responsive luciferase reporter (BRE-Luc) assay in LLC-PK1 cells[11,44]. Stimulation with 6 nM purified BMP2 increased BRE-luciferase activity ~5-fold (n=40, $P<0.0001$) over the control (Fig. 4g). When we transfected cells with full-length (GPI-anchored) RGMB, BRE luciferase activity was further enhanced ~3-fold (n=40, $P<0.0001$) (Fig. 4g), comparable to published results[11], whereas transfection with a GPI-anchored RGMB construct lacking the $RGMB_{ND}$ domain ($RGMB_{\Delta N}$) had no effect (n=40, $P=0.0509$) on the BMP-induced response (Fig. 4g). This confirmed that the N-terminal domain is necessary for this activation, in agreement with our structural and SPR analysis (Fig. 3d, e and Supplementary Fig. 4j).

Next, we investigated the effects of soluble proteins (lacking the membrane attachment sites) in the same luciferase reporter assay (Fig. 4h, and Supplementary Fig. 5). Stimulation with 6 nM purified BMP2 increased BRE-luciferase activity ~10-fold (n=72, $P<0.0001$) over the control (n=37) (Fig. 4h). When we transfected cells with soluble eBMPR1A, BRE luciferase activity decreased to ~75% (n=22, $P<0.0001$). In contrast, transfection with soluble eRGMB and $RGMB_{ND}$ did not reduce BRE luciferase activity (n=22, $P=0.8606$; n=24, $P=0.992$ respectively) (Fig. 4h, and Supplementary Fig. 5), contrasting with previous studies using a RGMB–Fc fusion construct[11]. To further validate our observation, we performed similar experiments, but now added purified eBMPR1A or eRGMB proteins directly to LLC-PK1 or C2C12 cells (Supplementary Fig. 5). Again, we observed inhibition of BMP signaling by eBMPR1A, whereas eRGMB did not inhibit BMP2 signaling in either

cell type, even at concentrations (2.5 μM) three times the K_d for the eRGMB–BMP2 interaction (Supplementary Fig. 5). In summary, soluble BMPR1A ectodomain acts as a "ligand-trap", competing with endogenous BMP type I receptors and inhibiting signaling, as expected. Surprisingly however, we found that this behavior does not extend to soluble RGMB proteins that nonetheless have similar binding affinities and can compete with the BMPR1A–BMP2 interaction. This finding, linked with the pH dependence of the RGMB–BMP2 interaction may imply an endocytosis-linked mechanism of RGM-activated BMP signaling.

The structure of the ternary BMP–RGM–NEO1 complex

To place the RGM–BMP2 interaction into the context of the RGM–NEO1 signaling hub[9], we next determined the crystal structure of the ternary complex composed of BMP2, eRGMB and the juxtamembrane region of NEO1 including the fifth (FN5) and sixth (FN6) fibronectin type III domains (Fig. 5a, b). In the complex, a disulfide-linked BMP2 dimer binds to two molecules of $RGMB_{ND}$ in a very similar arrangement to that observed in the binary BMP2–$RGMB_{ND}$ complex (r.m.s.d. of 0.799 Å for 328 equivalent Cα positions) (Supplementary Fig. 6a). Each $RGMB_{ND}$ is connected to the RGMB C-terminal domain ($RGMB_{CD}$) via a disordered 15 amino acid linker not visible in the electron density map. $RGMB_{CD}$ interacts with NEO1 via a similar mode to that observed for the major interaction site in the previously determined eRGMB–NEO1 complex structure[9] (r.m.s.d. of 0.511 Å for 368 equivalent Cα positions) (Supplementary Fig. 6a). In the ternary complex, the FN5 domain of NEO1 also contacts BMP2 (Fig. 5a). However, analysis of the observed interfaces (Supplementary Fig. 6b) suggests that this NEO1–BMP2 interaction is due to crystal packing rather than an important biological interface, which is in agreement with the fact that binding affinities of BMP2 to eRGMB or the purified eRGMB–NEO1 complex were similar and that there was no increase in affinity contributed by NEO1 (Supplementary Fig. 4k).

To test whether a similar arrangement of the RGMB–NEO1–BMP2 complex exists in solution we carried out small-angle X-ray scattering (SAXS) experiments of the eRGMB–NEO1–BMP2 complex and its components (Fig. 5c and Supplementary Fig. 7). The eRGMB–NEO1–BMP2 complex, prepared via size exclusion chromatography (Supplementary Fig. 7a, b), resulted in a particle of a mass consistent with the ternary complex in a 2:2:2 stoichiometry. Starting from the crystal structure, we generated ensembles of RGMB–NEO1–BMP2 models by molecular dynamics sampling and selected these against the SAXS data. The solution structure can be accurately described (χ^2=1.9) as a mixture of two models that have architectures similar to the crystal structure, but which show structural variation only at the level of the linker that connected $RGMB_{ND}$ and $RGMB_{CD}$, thereby dislocating the NEO1–FN5 domain away from BMP2 (Fig. 5c) and thus supporting our analysis of the observed interfaces in this complex interaction network (Supplementary Fig. 6b).

BMP mediates clustering of RGM–NEO1 at the cell surface

In the ternary complex, the two RGM and NEO1 molecules are orientated in such a way that the C-termini (that, in the context of the full-length proteins, are connected with the lipid

bilayer of the plasma membrane) point in the same direction (Fig. 5b). This arrangement, also observed in solution, combined with the active signaling conformation of the 2:2 complex between NEO1 and the C-terminal domain of RGM[9] suggests a mode of clustering in which RGM bridges the dimers of BMP and NEO1, respectively (Fig. 5d). Indeed, total internal reflection fluorescence microscopy (TIRFM) combined with direct stochastic optical reconstruction microscopy (dSTORM)[45] in COS7 cells (Fig. 6a, b) revealed an increase in the clustering of fluorescently-tagged NEO1 molecules in a time-dependent manner after the addition of 20 nM BMP2 using live (Fig. 6a–f) and fixed (Fig 6g, h) cells, respectively. This clustering was dependent on the presence of full-length RGMB and reached a maximum ~15 minutes after addition of BMP2 (Fig. 6e-h).

DISCUSSION

RGMs can signal through both trans (intercellular)[9] and cis (same cell) interactions. Cis signaling occurs in a BMP-dependent manner, such as in chondrocytes[46] and hepatocytes[14], when both NEO1 and RGM are expressed on the same cell surface. Although the role of NEO1 in BMP signaling is still unclear and cell type dependent[47], multiple lines of evidence point towards a central role for the NEO1–RGM interaction in controlling BMP ligand-receptor localization. In hepatocytes, NEO1 inhibits RGMC shedding, thus enhancing BMP signaling and hepcidin expression in the liver[13,14]. This is in agreement with our results where high local RGM concentrations were required for activation of BMP in a luciferase reporter assay (Fig. 4g, h), which are, *in vivo*, likely only provided by membrane attachment of RGMs to BMP-responsive cells. Furthermore, SMAD-dependent BMP signaling is reduced in chondrocytes in NEO1-deficient mice, further suggesting that NEO1 regulates BMP receptor localization with RGMs potentially acting as a protein scaffold that could support a BMP receptor super-complex in membrane microdomains[46]. It is interesting to note that NEO1 is located in membrane microdomains in growth cones of axons, a process that is dependent on the presence of both RGM and BMP signaling[48]. Our structural and functional data identifies the RGM N-terminal domain as being the site of direct interaction for the BMP ligand. This interaction is accommodated in the multi-domain architecture of our NEO1–RGM–BMP2 ternary complex structure, which allows simultaneous binding of RGMs to NEO1 and BMP ligands and results in RGM-mediated clustering by bridging dimers of NEO1 and BMP2.

Our luciferase reporter data, together with the pH-dependence of the RGMB–BMP2 interaction, suggests a potential mechanism for RGM-mediated activation of BMP signaling. We showed that soluble eBMPR1A acts as an inhibitor of BMP signaling, whereas eRGMB does not. We propose that this difference is linked to the pH-dependence of the RGMB–BMP2 interaction and the subcellular localization of the BMP signaling complexes. Upon clathrin-mediated endocytosis BMP2–RGMB complexes might be targeted into endosomes, which are enriched with BMP type I receptors[22]. The acidification of the endosomes might then promote dissociation of RGMB from the complex and replacement by the BMP type I receptor leading to enhanced BMP signals, due to potentiation of SMAD signaling provided by the endosomal environment compared to the cell surface[21,22]. In this scenario, the RGM–NEO1 complex could act as a shuttle for the BMP ligand (and potentially BMP type II receptors, which can be accommodated in our RGM–NEO1–BMP complex). The RGM–

NEO1 complex potentially sequesters the BMP ligand at the membrane, priming it for transport via endosomal pathways. Future work will be required to test our hypothesis, linking RGMs to BMP endocytosis, and to characterize this in different biological contexts. Translocation of the signaling machinery through established pathways to place it in close proximity to the nucleus, and thus downstream effector targets, is a very efficient way of effecting changes in gene expression. This mechanism has been suggested for other signaling pathways including the closely related TGFβ signaling[21] as well as epidermal growth factor (EGF)[49] and glial-cell derived neurotrophic factor (GDNF) signaling[50]. The molecular mechanism of RGM-mediated BMP activation, based on endocytosis of the entire signaling complex may provide a paradigm for many “cell-surface” signaling events.

ONLINE METHODS

Expression and purification of RGMs, NEO1 and BMP receptor constructs

Constructs of the extracellular region of human RGMA (GenBank ID AL136826, $RGMA_{ND}$: 45–139), human RGMB (GenBank ID AK074887, eRGMB: 53–412, $RGMB_{ND}$: 53–136, RGMB–ΔN: 137-412) human RGMC (GenBank ID AY372521, eRGMC: 36–400, $RGMC_{ND}$: 36–147), human BMPR1A (GenBank ID AK291764, eBMPR1A: 49–141), human ACVR2A (GenBank ID X63128, eACVR2A: 27–118), human BMPR2 (GenBank ID Z48923, eBMPR2: 33–132) and mouse NEO1 (GenBank ID Y09535; NEO1: 37–1493, $NEO1_{FN56}$: 883–1083 (ref. 54), $NEO1_{FN56M}$: 883–1134 (ref. 54)), fused C-terminally with either a hexa-histidine, a BirA recognition sequence or a mVenus tag, were cloned into the pHLsec vector[55] and expressed by transient transfection in HEK-293T cells (ATCC CRL-11268) (using a semi-automated procedure[56]) in the presence of the class I α-mannosidase inhibitor, kifunensine[57]. Five days post-transfection, the conditioned medium was dialyzed (48 h, 4 °C) against PBS and the proteins were purified by immobilized metal-affinity chromatography using TALON beads (Clontech) and, for crystallization, treated with endoglycosidase F1 (75 μg mg^{-1} protein, 12 h, 21 °C) to cleave glycosidic bonds of N-linked sugars resulting in only one N-acetyl-glucosamine moiety bound to the corresponding asparagine side chain. The proteins were concentrated and further purified by size-exclusion chromatography (SEC) (Superdex 200 16/60 column, GE Healthcare) in buffer containing 10 mM HEPES, pH 7.5, 150 mM NaCl. The production of $NEO1_{FN56}$ and $NEO1_{FN56M}$ followed a protocol described in[54].

Expression and purification of BMP2 and formation of protein complexes

BMP2 was expressed as inclusion bodies and purified as follows (protocol adapted from[58]). After cell lysis, inclusion body pellets were washed four times with 20 mM EDTA, 2% (v/v) Triton X-100, 500 mM NaCl, pH 7 and then solubilized in 6 M guanidinium hydrochloride (GdmHCl), 0.1 M Tris-HCl, pH 8.5, 1 mM EDTA and 100 mM DTT. The pH was dropped to 3–4 to inhibit disulfide bond formation. Residual insoluble material was removed by centrifugation (10 min, 10,000 g, 4 °C). DTT was removed by dialysis four times against 10- to 20-fold volume of 6 M GdmHCl, pH 3–4. Refolding was carried out by incubating the reduced and solubilized inclusion body preparation (24 h, 4 °C, ~200 μg/ml concentration) in 100 mM Tris-HCl, 5 mM EDTA, 1 M L-arginine, pH 8.3, 100 μM oxidized glutathione (GSSG), 100 μM reduced glutathione (GSH). The sample was

concentrated to 1 mg/ml using Amicon pressure filtration (Millipore) and the reaction split into two halves, one of which was oxidized with 25 mM GSSG (3 h, 4 °C). Excess GSSG was removed by dialysis and the two reaction halves were combined. This sample was concentrated and applied to a heparin column (5 ml HiTrap Heparin HP, GE Healthcare) followed by SEC in 4 M Urea, 100 mM Tris-HCl, pH 6.0, 5 mM EDTA. SEC fractions were analyzed by non-reducing SDS-PAGE and those with a purity > 95% of the dimeric species were pooled. BMP2-RGM_{ND} complexes were formed by mixing the proteins in a 1:1 molar ratio. For the tertiary BMP2-eRGMB-$NEO1_{FN56}$ complex, BMP2 was mixed in equimolar amounts with a previously SEC-purified eRGMB-$NEO1_{FN56}$ complex. The complex mixtures were incubated for 1 hour at room temperature prior to crystallization and concentrated to the appropriate concentration.

Site directed mutagenesis

Site-directed mutagenesis of RGM proteins to test specificity of protein-protein interactions was carried out by two-step, overlap-extension PCR using Pyrobest Polymerase (Takara). PCR products were cloned into the pHLsec vector as above[55]. Mutant RGM proteins were secreted at similar levels to the respective wildtype constructs (data not shown). The stringent quality control mechanisms specific to the mammalian cell secretory pathway is likely to ensure that secreted proteins are correctly folded[59].

Crystallization and data collection

Prior to crystallization, complexes were concentrated ($RGMA_{ND}$–BMP2: 6 mg/ml, $RGMB_{ND}$–BMP2: 6 mg/ml, $RGMC_{ND}$–BMP2: 5 mg/ml and BMP2–eRGMB–$NEO1_{FN56}$: 5 mg/ml). Crystallization trials, using 100 nl protein solution plus 100 nl reservoir solution in sitting drop vapor diffusion format were set up in 96-well Greiner plates using a Cartesian Technologies robot[60]. Crystallization plates were maintained at 6.5 or 20.0 °C in a TAP Homebase storage vault and imaged via a Veeco visualization system[61]. All binary RGM–BMP2 complex crystals were grown at 6.5 °C, whereas the ternary BMP2–eRGMB–$NEO1_{FN56}$ complex was crystallized at 20 °C. $RGMA_{ND}$–BMP2 crystals were obtained out of mother liquor containing 0.1 M citric acid, pH 4.0, 20% (v/v) 2-methyl-2,4-pentanediol (MPD), 0.2 M glycine, $RGMB_{ND}$–BMP2 Form-1 crystals out of 2 M ammonium sulfate, 8% (v/v) 2,5-hexanediol, $RGMB_{ND}$–BMP2 Form-2 crystals out of 0.08 M citric acid, pH 4.0, 15% (v/v) MPD, $RGMC_{ND}$–BMP2 crystals out of 20% (w/v) PEG3350, 0.2 M ammonium nitrate and BMP2–eRGMB–$NEO1_{FN56}$ crystals out of 0.1 M Tris-HCl, pH 8.5, 1.5 M ammonium sulfate, 12% (v/v) glycerol. Diffraction data were collected at 100 K at the following wavelengths: $RGMA_{ND}$–BMP2: 1.0163 Å, $RGMB_{ND}$–BMP2 Form 1: 0.97620 Å, $RGMB_{ND}$–BMP2 Form 2: 0.91730 Å, $RGMC_{ND}$–BMP2: 0.97625 Å, BMP2–eRGMB–$NEO1_{FN56}$: 0.97625 Å. Prior to flash-freezing, crystals were treated with the appropriate cryo-protectant solutions ($RGMA_{ND}$–BMP2 and $RGMB_{ND}$–BMP2 Form-2: 30% (v/v) MPD in mother liquor; $RGMB_{ND}$–BMP2 Form-1 and $RGMC_{ND}$–BMP2: 30% (v/v) ethylene glycol in mother liquor; BMP2–eRGMB–$NEO1_{FN56}$: 15% (v/v) glycerol in mother liquor). Data were collected at beamline I03 ($RGMA_{ND}$–BMP2, $RGMB_{ND}$–BMP2 Form-1, $RGMC_{ND}$–BMP2), I04 (BMP2–eRGMB–$NEO1_{FN56}$) and I04-1 ($RGMB_{ND}$–BMP2 Form-2) at the Diamond Light Source, UK. X-ray data were processed and scaled with the HKL suite[62] and XIA2[63-68]. Data collection statistics are shown in Table 1.

Structure determination and refinement

The $RGMC_{ND}$–BMP2 complex was solved by molecular replacement in PHASER[69] using the structure of the disulfide bonded BMP2 dimer (PDB 3BMP[70]) as a search model. Extra electron density for two molecules of $RGMC_{ND}$ in the asymmetric unit was immediately discernible after density modification in PARROT[71] (Supplementary Fig. 2a, b). The RGMC polypeptide chain was traced using iterative rounds of BUCCANEER[72], manual building in COOT[73] and refinement in autoBUSTER[74] and PHENIX[75]. This resulted in a well-defined model for the $RGMC_{ND}$–BMP2 complex that included two molecules of RGMC (residues Q36–P129) bound to a disulfide linked BMP2 dimer (residues K293–R396) (Supplementary Fig. 2c). The $RGMA_{ND}$–BMP2 and $RGMB_{ND}$–BMP2 complexes were solved by molecular replacement using PHASER with the $RGMC_{ND}$–BMP2 complex as a search model. Molecular replacement with PHASER was applied to solve the BMP2–eRGMB–$NEO1_{FN56}$ structure using the $RGMB_{ND}$–BMP2 Form 1 (from this study) and the $NEO1_{FN56}$–RGMB (PDB ID. 4BQ6[54]) structures. The complexes were refined using autoBUSTER[74] and PHENIX[75] and, where applicable, non-crystallographic restraints were applied. For the BMP2–eRGMB–$NEO1_{FN56}$ structure target weight refinement using the individual high resolution structures of the BMP2, $RGMB_{ND}$, eRGMB, $NEO1_{FN5}$ and $NEO1_{FN6}$ domains as targets was applied. Crystallographic statistics are given in Table 1. Stereochemical properties were assessed by MOLPROBITY[76]. Superpositions were calculated using the program COOT[73] and electrostatic potentials were generated using APBS[77] as implemented in PYMOL[78]. Buried surface areas of protein-protein interactions were calculated using the PISA webserver[79] for a probe radius of 1.4 Å.

Small-Angle X-ray scattering (SAXS)

Data were collected at beamline BM29 of the European Synchrotron Radiation Facility (ESRF, Grenoble, France)[80] at 293 K within a momentum transfer (q) range of 0.01 $Å^{-1} < q < 0.45$ $Å^{-1}$, where $q = 4\pi\sin(\theta)/\lambda$ and 2θ is the scattering angle. X-ray wavelength was 0.0995 nm and data were collected on a Pilatus 1M detector. Protein samples were measured at the following concentrations: $NEO1_{FN56M}$: 1.06 and 4.94 mg/ml, eRGMB: 0.96 and 5.48 mg/ml, $NEO1_{FN56M}$–eRGMB: 0.51 and 1.01 mg/ml, and BMP2–eRGMB–$NEO1_{FN56M}$: 0.68 and 1.14 mg/ml. Data reduction and calculation of invariants was carried out using the ATSAS software suite[81]. A merged dataset was obtained by combining the low-angle part of the low-concentration dataset with the high-angle part of the high-concentration dataset. Molecular weight determination was performed using the volume of correlation metric V_C using Scatter[82]. The BMP2–eRGMB–$NEO1_{FN56M}$ solution structure was modeled starting from the crystal structure of the ternary complex. A structural model for C-terminal eRGMB residues His335–Ser410 (not observed in the electron density) was calculated using ROSETTA3.5 (ref. 83), constrained by imposing alpha-helical secondary structure and a disulfide bond between Cys358 and Cys372. Missing loops and N- and C-termini were added in extended conformations using Modeller[84]. Starting models for $NEO1_{FN56M}$, eRGMB, and the eRGMB–$NEO1_{FN56M}$ binary subcomplex were then extracted from the completed BMP2-eRGMB–$NEO1_{FN56M}$ model. All-atom ensemble modeling of $NEO1_{FN56M}$, eRGMB, eRGMB–$NEO1_{FN56M}$ and BMP2–eRGMB–$NEO1_{FN56M}$ was performed using AllosMod[85]; and in each case, 50 independent ensembles of 100 models

were generated. From this pool, automated selection of the minimal set of models satisfying the scattering data was performed using MES[86], and calculation and fitting of scattering patterns was performed using FoXS[87]. This procedure was automated using the AllosMod-FoXS web server[88]. The solution structures of $NEO1_{FN56M}$, eRGMB, eRGMB–$NEO1_{FN56M}$ and BMP2–eRGMB–$NEO1_{FN56M}$ are described by one, one, three and two models, respectively.

Multiangle light scattering (MALS)

MALS experiments were carried out using a DAWN HELEOS II (Wyatt Technology), equipped with a K5 flow cell and a 30 mW linearly polarized GaAs laser with a wavelength of 690 nm. Proteins used for MALS contained wild-type sugars. Proteins were purified by SEC and the BMP2–$RGMB_{ND}$ and BMP2–eBMPR1A complexes were formed by mixing the components in a 1:1 molar ratio. Complexes were dialyzed against buffers generated using the MMT buffer system (**M**alic acid, **M**ES, **T**ris; Molecular Dimensions): 10 mM MMT, pH 5.5/6.5/7.5, 150 mM NaCl. Complexes were concentrated to 2 mg/ml prior to MALS analysis. Data were analyzed using ASTRA (Wyatt Technologies) and molecular weights were calculated using the Debye fit method. Molecular weights were calculated as: BMP2–$RGMB_{ND}$/pH 7.5: 46.2±2.7, 22.4±0.9; BMP2–$RGMB_{ND}$/pH 6.5: 20.1±1.4, 13.4±0.4; BMP2–$RGMB_{ND}$/pH 5.5: 24.0±1.2, 16.2±0.3; BMP2–eBMPR1A/pH 7.5: 53.0±0.1, 15.0±0.2; BMP2–eBMPR1A/pH 6.5: 53.2±0.3, 18.8±0.1; BMP2–eBMPR1A/pH 5.5: 54.2±0.5, 19.7±0.4. These molecular weights correspond to the calculated masses: BMP2–$RGMB_{ND}$: 47 kDa, BMP2: 26 kDa, $RGMB_{ND}$: 11 kDa, BMP2–eBMPR1a: 53 kDa, eBMPR1a: 14 kDa. Graphs were produced using GraphPad Prism Version 6.04 (GraphPad Software, La Jolla California USA).

Surface plasmon resonance (SPR) binding studies

SPR experiments were performed using a BIAcore T200 machine (GE Healthcare) at 25 °C in SPR running buffer (10 mM HEPES, pH 7.5, 150 mM NaCl, 0.005% (v/v) polysorbate 20). All experiments were performed using direct protein immobilization by amine coupling to CM5 biosensor chips except for Supplementary Fig. 4p-r, where biotinylated eRGMB was immobilized onto streptavidin-coupled CM5 biosensor chips[89]. Analytes were dialyzed against SPR running buffer prior to use, and 1 in 2 dilution series were prepared. For the competition experiment a 1 in 2 dilution series of a mixture of 20 μM eBMPR1A and 2.5 μM eRGMB was prepared in buffer containing 2.5 μM eRGMB, resulting in a dilution series of eBMPR1A in a constant (2.5 μM) concentration of eRGMB. BMP2 surface concentrations were 150, 500 and 1000 response units. Surfaces coupled with BMP2 were regenerated by bursts of 4 M Urea, 50 mM Tris pH 8.0, 150 mM NaCl (120s, 20 μl/min) and the experimental trace returned to baseline. In all experiments error range, s.e.m. (n = 2 technical replicates). The signal from experimental flow cells was corrected by subtraction of the nearest blank injection and the reference signal from a blank flow cell. All data were analyzed using SCRUBBER2 (Biologic) and GraphPad Prism Version 6.04 (GraphPad Software, La Jolla California USA). Best-fit binding curves were calculated for BMP2 – BMP receptor interactions using non-linear curve fitting of a “one-site specific binding” model ($Y=B_{max}*X/(K_d+X)$, X=analyte concentration, B_{max}=maximum analyte binding). For BMP2–RGM binding, best-fit curves were calculated using non-linear curve fitting of a

"one-site total binding" model ($Y=B_{max}*X/(K_d+X)+NS*X+Background$, X=analyte concentration, Background=0 as data were already referenced), non-specific binding is proportional to analyte concentration and therefore NS is the slope of non-specific binding. B_{max} and K_d values were determined for the specific binding component only. For the eBMPR1A–eRGMB competition experiment a best-fit binding curve was calculated using a "log(agonist) vs response variable slope" model (Y=Bottom+(Top-Bottom)/(1+10^((LogEC50–X)*HillSlope)), X=analyte concentration, top=Y_{max}, bottom=Y_{min}, EC50 is the concentration of agonist that gives a response half way between bottom and top). The HillSlope parameter was constrained to 1.0. An R^2 value to quantify goodness of fit (range 0–1.0) and an IC_{50} value were reported.

Luciferase reporter assay

LLC-PK1 cells, or C2C12 cells stably transfected with a BRE-luciferase reporter plasmid[90], were plated in complete DMEM supplemented with 10% FBS at a density of 5×10^4 cells/ml in a 96-well plate (100 µl/well) (Nunc-Immuno™ MicroWell™ 96 well polystyrene plates, Sigma-Aldrich). After 24 h LLC-PK1 cells were transfected using Lipofectamine 2000 transfection reagent (Lifetechnologies) according to manufacturer's protocol, with 40 ng pGL3 BRE-Luciferase plasmid[91], 30 ng Renilla control plasmid and, where indicated, 20 ng of empty pHLSec vector control or test constructs as indicated. Eight hours post-transfection the cells were washed with PBS (100 µl) and serum starved in complete DMEM supplemented with 0.1% FBS overnight. Cells were stimulated with 6 nM, 10 nM or 25 nM BMP2 as indicated or buffer. Where soluble proteins were directly added to the cells, BMP2 was pre-incubated with a dilution series (from 0.4–100 × the molar concentration of BMP2) of eBMPR1A or eRGMB. After 48 hours incubation, cells were washed with PBS, lysed, and luciferase activity measured using a dual luciferase assay system (Promega) according to the manufacturer's instructions. Luminescence was quantified using a luminometer (Tecan, Infinite 200 PRO). Graphs were produced and statistical tests carried out using GraphPad Prism Version 6.04 (GraphPad Software, La Jolla California USA).

Sample Preparation for microscopy

Prior to imaging 40 nM BMP2 solution was dialyzed against phenol red-free complete DMEM supplemented with 0.1 % FBS to remove 10 mM ammonium acetate buffer. COS7 cells were seeded at a density of 1×10^5 cells/ml in glass bottom dishes (2 ml) (MatTek). After 24 hours, cells were transfected with 1.5 µg NEO1-mVenus and 1.5 µg full-length RGMB using Lipofectamine 2000 transfection reagent (Lifetechnologies) according to the manufacturer's protocol. Eight hours post-transfection the cells were serum-starved in phenol red-free complete DMEM supplemented with 0.1% FBS overnight. Prior to imaging cell media was replaced with either 20 nM BMP2-containing media or blank media. Live-cell imaging was carried out immediately. For fixed samples, the BMP2 or blank media was removed after the indicated amount of time, cells were fixed with 4 % paraformaldehyde (PFA) (10 min, room temperature) and washed thoroughly in PBS to remove excess PFA before being stored in PBS at 4 °C.

Imaging

Images were acquired on a total internal reflection fluorescence microscope (TIRFM) (ELYRA; Zeiss) with a 100× oil-immersion objective with a numerical aperture of 1.46. For illumination/photoconversion, 30% transmission of the 488-nm laser and 1% transmission of the 405-nm laser were used and 5,000–10,000 images were acquired per sample with a cooled, electron-multiplying charge-coupled device camera (iXon DU-897D; Andor). Exposure time was 300 ms. Recorded images were analyzed with Zeiss ZEN software.

dSTORM Data Processing

Raw fluorescence intensity images were analyzed using the software Zen 2010D (Zeiss MicroImaging). A Gaussian and Laplace filter was applied to each frame, and overlapping events were excluded. An event was classified as originating from a single molecule when $I - M > 6S$ (I is event intensity, M is mean image intensity and S is the s.d. of image intensity). The center of each point-spread function was then calculated by fitting to a two-dimensional Gaussian distribution and a table containing the *x*-*y* particle coordinates of each molecule was extracted. Regions of interest, 5 μm × 5 μm or 3 μm × 3 μm in area, containing the two-dimensional molecular coordinates were cropped for analysis using Origin (Northhampton, MA, USA), and events with localization precision worse than 60 nm were discarded. Areas containing ~300 molecules for live cell imaging and ~1000 events for the fixed samples were selected. To analyze the spatial point pattern, we used the Ripley's *K*-function, calculated with SpPack[92] and the *Spatstat package* for R software[93], and plotted the L-function as described[94,95]. Briefly, Ripley's *K*-function is a measure of the number of points encircled by concentric circles of radius *r* centered on each point. K-values from the Ripley function therefore scale with circle area and so are transformed into the *L*-function. Using this equation, scaling is linear with the radius. Random distributions have an $L(r)$ value of r over all r values. Therefore to analyze levels of clustering we plotted $L(r)$ against r; and positive values at a given r indicate clustering at that spatial scale. Quantitative cluster maps were generated using Getis and Frankin's analysis as described[94,95]. Briefly, $L(r)$ values at a spatial scale of 50 nm (L(50)) were computed for each point with R and interpolated using Origin to produce a quantitative cluster map. This was then pseudo-colored with ImageJ[96] to highlight regions of high clustering. Live cell dSTORM images were constructed using a time-gated window approach[97,98]. On the basis of the frame number from the raw data acquisition, cluster maps were generated from 5000 continuous frames, with each cluster map shifted by 2000 frames relative to the previous one. This corresponded to a time-gated window of ~7 minutes with the clustering analyzed over a total of 30 minutes.

Illustrations

Figures were produced using the programs PYMOL[78], Adobe Photoshop (Adobe Systems), ImageJ[96] and Corel Draw (Corel Corporation). Sequence alignments were conducted using MULTALIN (bioinfo.genotoul.fr/multalin/multalin.html) and formatted with ESPRIPT (espript.ibcp.fr/ESPript/ESPript/).

Supplementary Material

Refer to Web version on PubMed Central for supplementary material.

ACKNOWLWEDGEMENTS

We thank the staff of beamlines I03, I04 and I04-1 at the Diamond Light Source, UK (X-ray diffraction data, proposal MX-10627), BM29 at the ESRF, France (SAXS data) and the Cellular Imaging Core at the WTCHG Oxford, UK (TIRF and dSTORM data) for assistance, T. Walter and K. Harlos for help with crystallization, R. Robinson and G. Sutton with MALS and A.R. Aricescu and D.I. Stuart for reading the manuscript. This work was supported by Cancer Research UK (C20724/A14414) and the Wellcome Trust (097301/Z/11/Z). Further support from the Wellcome Trust Core Award Grant 090532/Z/09/Z and the Wellcome Trust Multi-User Equipment Grant 101584MA (S.P.-P., C.S.) are acknowledged. E.G.H. is funded by a Wellcome Trust PhD studentship. J.E. is a Marie-Curie Postdoctoral fellow (FP7-328531). S.P.-P. is a Nuffield Department of Medicine Leadership Fellow. C.S. is a Cancer Research UK Senior Research Fellow.

References

1. Yamashita T, Mueller BK, Hata K. Neogenin and repulsive guidance molecule signaling in the central nervous system. Curr Opin Neurobiol. 2007; 17:29–34. [PubMed: 17169551]
2. Mirakaj V, et al. Repulsive guidance molecule-A (RGM-A) inhibits leukocyte migration and mitigates inflammation. Proc Natl Acad Sci U S A. 2011; 108:6555–60. [PubMed: 21467223]
3. Muramatsu R, et al. RGMa modulates T cell responses and is involved in autoimmune encephalomyelitis. Nat Med. 2011; 17:488–94. [PubMed: 21423182]
4. Li VS, et al. Frequent inactivation of axon guidance molecule RGMA in human colon cancer through genetic and epigenetic mechanisms. Gastroenterology. 2009; 137:176–87. [PubMed: 19303019]
5. Papanikolaou G, et al. Mutations in HFE2 cause iron overload in chromosome 1q-linked juvenile hemochromatosis. Nat Genet. 2004; 36:77–82. [PubMed: 14647275]
6. Monnier PP, et al. RGM is a repulsive guidance molecule for retinal axons. Nature. 2002; 419:392–5. [PubMed: 12353034]
7. Rajagopalan S, et al. Neogenin mediates the action of repulsive guidance molecule. Nat Cell Biol. 2004; 6:756–62. [PubMed: 15258590]
8. Matsunaga E, Chedotal A. Repulsive guidance molecule/neogenin: a novel ligand-receptor system playing multiple roles in neural development. Dev Growth Differ. 2004; 46:481–6. [PubMed: 15610137]
9. Bell CH, et al. Structure of the Repulsive Guidance Molecule (RGM)–Neogenin Signaling Hub. Science. 2013
10. Babitt JL, et al. Bone morphogenetic protein signaling by hemojuvelin regulates hepcidin expression. Nat Genet. 2006; 38:531–539. [PubMed: 16604073]
11. Samad TA, et al. DRAGON, a bone morphogenetic protein co-receptor. J Biol Chem. 2005; 280:14122–9. [PubMed: 15671031]
12. Babitt JL, et al. Repulsive Guidance Molecule (RGMa), a DRAGON Homologue, Is a Bone Morphogenetic Protein Co-receptor. J Biol Chem. 2005; 280:29820–29827. [PubMed: 15975920]
13. Lee DH, et al. Neogenin inhibits HJV secretion and regulates BMP-induced hepcidin expression and iron homeostasis. Blood. 2010; 115:3136–45. [PubMed: 20065295]
14. Zhang AS, Yang F, Wang J, Tsukamoto H, Enns CA. Hemojuvelin-neogenin interaction is required for bone morphogenic protein-4-induced hepcidin expression. J Biol Chem. 2009; 284:22580–9. [PubMed: 19564337]
15. Massague J. TGFbeta signalling in context. Nat Rev Mol Cell Biol. 2012; 13:616–30. [PubMed: 22992590]
16. Sieber C, Kopf J, Hiepen C, Knaus P. Recent advances in BMP receptor signaling. Cytokine Growth Factor Rev. 2009; 20:343–55. [PubMed: 19897402]
17. Bragdon B, et al. Bone morphogenetic proteins: a critical review. Cell Signal. 2011; 23:609–20. [PubMed: 20959140]
18. Shi Y, Massague J. Mechanisms of TGF-beta signaling from cell membrane to the nucleus. Cell. 2003; 113:685–700. [PubMed: 12809600]
19. Feng XH, Derynck R. Specificity and versatility in tgf-beta signaling through Smads. Annu Rev Cell Dev Biol. 2005; 21:659–93. [PubMed: 16212511]

20. Derynck R, Zhang YE. Smad-dependent and Smad-independent pathways in TGF-beta family signalling. Nature. 2003; 425:577–84. [PubMed: 14534577]
21. Di Guglielmo GM, Le Roy C, Goodfellow AF, Wrana JL. Distinct endocytic pathways regulate TGF-beta receptor signalling and turnover. Nat Cell Biol. 2003; 5:410–21. [PubMed: 12717440]
22. Hartung A, et al. Different Routes of Bone Morphogenic Protein (BMP) Receptor Endocytosis Influence BMP Signaling. Mol Cell Biol. 2006; 26:7791–7805. [PubMed: 16923969]
23. Heining E, Bhushan R, Paarmann P, Henis YI, Knaus P. Spatial segregation of BMP/Smad signaling affects osteoblast differentiation in C2C12 cells. PLoS One. 2011; 6:e25163. [PubMed: 21998639]
24. Alborzinia H, et al. Quantitative kinetics analysis of BMP2 uptake into cells and its modulation by BMP antagonists. J Cell Sci. 2013; 126:117–127. [PubMed: 23077176]
25. Shi W, et al. Endofin acts as a Smad anchor for receptor activation in BMP signaling. J Cell Sci. 2007; 120:1216–24. [PubMed: 17356069]
26. Brazil DP, Church RH, Surae S, Godson C, Martin F. BMP signalling: agony and antagony in the family. Trends Cell Biol. 2015
27. Xia Y, et al. Dragon (repulsive guidance molecule b) inhibits IL-6 expression in macrophages. J Immunol. 2011; 186:1369–76. [PubMed: 21187450]
28. Lee PL, Beutler E, Rao SV, Barton JC. Genetic abnormalities and juvenile hemochromatosis: mutations of the HJV gene encoding hemojuvelin. Blood. 2004; 103:4669–71. [PubMed: 14982867]
29. Lok CY, et al. Iron overload in the Asian community. Blood. 2009; 114:20–5. [PubMed: 19342478]
30. Parrow NL, Fleming RE. Bone morphogenetic proteins as regulators of iron metabolism. Annu Rev Nutr. 2014; 34:77–94. [PubMed: 24995692]
31. Yang F, West AP Jr. Allendorph GP, Choe S, Bjorkman PJ. Neogenin interacts with hemojuvelin through its two membrane-proximal fibronectin type III domains. Biochemistry. 2008; 47:4237–45. [PubMed: 18335997]
32. Wu Q, Sun CC, Lin HY, Babitt JL. Repulsive guidance molecule (RGM) family proteins exhibit differential binding kinetics for bone morphogenetic proteins (BMPs). PLoS One. 2012; 7:e46307. [PubMed: 23029472]
33. Xiong JP, et al. Crystal structure of the extracellular segment of integrin alpha Vbeta3 in complex with an Arg-Gly-Asp ligand. Science. 2002; 296:151–5. [PubMed: 11884718]
34. Camus LM, Lambert LA. Molecular evolution of hemojuvelin and the repulsive guidance molecule family. J Mol Evol. 2007; 65:68–81. [PubMed: 17593421]
35. Kuns-Hashimoto R, Kuninger D, Nili M, Rotwein P. Selective binding of RGMc/hemojuvelin, a key protein in systemic iron metabolism, to BMP-2 and neogenin. Am J Physiol Cell Physiol. 2008; 294:C994–C1003. [PubMed: 18287331]
36. Roetto A, et al. Mutant antimicrobial peptide hepcidin is associated with severe juvenile hemochromatosis. Nat Genet. 2003; 33:21–2. [PubMed: 12469120]
37. Weinstein DA, et al. Inappropriate expression of hepcidin is associated with iron refractory anemia: implications for the anemia of chronic disease. Blood. 2002; 100:3776–81. [PubMed: 12393428]
38. Pagani A, Silvestri L, Nai A, Camaschella C. Hemojuvelin N-terminal mutants reach the plasma membrane but do not activate the hepcidin response. Haematologica. 2008; 93:1466–72. [PubMed: 18827264]
39. Allendorph GP, Vale WW, Choe S. Structure of the ternary signaling complex of a TGF-beta superfamily member. Proc Natl Acad Sci U S A. 2006; 103:7643–8. [PubMed: 16672363]
40. Weber D, et al. A silent H-bond can be mutationally activated for high-affinity interaction of BMP-2 and activin type IIB receptor. BMC Struct Biol. 2007; 7:6. [PubMed: 17295905]
41. Townson SA, et al. Specificity and structure of a high affinity activin receptor-like kinase 1 (ALK1) signaling complex. J Biol Chem. 2012; 287:27313–25. [PubMed: 22718755]
42. Heinecke K, et al. Receptor oligomerization and beyond: a case study in bone morphogenetic proteins. BMC Biology. 2009; 7:59. [PubMed: 19735544]

43. Keller S, Nickel J, Zhang J-L, Sebald W, Mueller TD. Molecular recognition of BMP-2 and BMP receptor IA. Nat Struct Mol Biol. 2004; 11:481–488. [PubMed: 15064755]
44. Korchynskyi O, ten Dijke P. Identification and functional characterization of distinct critically important bone morphogenetic protein-specific response elements in the Id1 promoter. J Biol Chem. 2002; 277:4883–91. [PubMed: 11729207]
45. Rossy J, Owen DM, Williamson DJ, Yang Z, Gaus K. Conformational states of the kinase Lck regulate clustering in early T cell signaling. Nat Immunol. 2013; 14:82–9. [PubMed: 23202272]
46. Zhou Z, et al. Neogenin regulation of BMP-induced canonical Smad signaling and endochondral bone formation. Dev Cell. 2010; 19:90–102. [PubMed: 20643353]
47. Xia Y, Babitt JL, Sidis Y, Chung RT, Lin HY. Hemojuvelin regulates hepcidin expression via a selective subset of BMP ligands and receptors independently of neogenin. Blood. 2008; 111:5195–204. [PubMed: 18326817]
48. Tassew NG, et al. Modifying lipid rafts promotes regeneration and functional recovery. Cell Rep. 2014; 8:1146–59. [PubMed: 25127134]
49. Vieira AV, Lamaze C, Schmid SL. Control of EGF receptor signaling by clathrin-mediated endocytosis. Science. 1996; 274:2086–9. [PubMed: 8953040]
50. Le Roy C, Wrana JL. Clathrin- and non-clathrin-mediated endocytic regulation of cell signalling. Nat Rev Mol Cell Biol. 2005; 6:112–26. [PubMed: 15687999]
51. Weiss MS. Global indicators of X-ray data quality. J. of Appl. Cryst. 2001; 34:130–135.
52. Karplus PA, Diederichs K. Linking crystallographic model and data quality. Science. 2012; 336:1030–3. [PubMed: 22628654]
53. Evans PR, Murshudov GN. How good are my data and what is the resolution? Acta Crystallogr D Biol Crystallogr. 2013; 69:1204–14. [PubMed: 23793146]

Methods References

54. Bell CH, et al. Structure of the Repulsive Guidance Molecule (RGM)–Neogenin Signaling Hub. Science. 2013; 341:77–80. [PubMed: 23744777]
55. Aricescu AR, Lu W, Jones EY. A time- and cost-efficient system for high-level protein production in mammalian cells. Acta Crystallogr D Biol Crystallogr. 2006; 62:1243–1250. [PubMed: 17001101]
56. Zhao Y, et al. Automation of large scale transient protein expression in mammalian cells. J Struct Biol. 2011; 175:209–215. [PubMed: 21571074]
57. Chang VT, et al. Glycoprotein structural genomics: solving the glycosylation problem. Structure. 2007; 15:267–273. [PubMed: 17355862]
58. von Einem S, Schwarz E, Rudolph R. A novel TWO-STEP renaturation procedure for efficient production of recombinant BMP-2. Protein Expr Purif. 2010; 73:65–69. [PubMed: 20302941]
59. Trombetta ES, Parodi AJ. Quality control and protein folding in the secretory pathway. Annu Rev Cell Dev Biol. 2003; 19:649–676. [PubMed: 14570585]
60. Walter TS, et al. A procedure for setting up high-throughput nanolitre crystallization experiments. Crystallization workflow for initial screening, automated storage, imaging and optimization. Acta Crystallogr D Biol Crystallogr. 2005; 61:651–657. [PubMed: 15930615]
61. Mayo CJ, et al. Benefits of automated crystallization plate tracking, imaging, and analysis. Structure. 2005; 13:175–182. [PubMed: 15698562]
62. Otwinowski Z, Minor W. Processing of X-ray diffraction data collected in oscillation mode. Methods Enzymol. 1997; 276:307–326.
63. Evans P. Scaling and assessment of data quality. Acta Crystallographica Section D. 2006; 62:72–82.
64. Kabsch W. Automatic indexing of rotation diffraction patterns. Journal of Applied Crystallography. 1988; 21:67–72.
65. Kabsch W. Automatic processing of rotation diffraction data from crystals of initially unknown symmetry and cell constants. Journal of Applied Crystallography. 1993; 26:795–800.

66. Leslie AGW. The integration of macromolecular diffraction data. Acta Crystallogr D Biol Crystallogr. 2006; 62:48–57. [PubMed: 16369093]
67. Sauter NK, Grosse-Kunstleve RW, Adams PD. Robust indexing for automatic data collection. Journal of Applied Crystallography. 2004; 37:399–409. [PubMed: 20090869]
68. Zhang Z, Sauter NK, van den Bedem H, Snell G, Deacon AM. Automated diffraction image analysis and spot searching for high-throughput crystal screening. Journal of Applied Crystallography. 2006; 39:112–119.
69. McCoy AJ, et al. Phaser crystallographic software. Journal of Applied Crystallography. 2007; 40:658–674. [PubMed: 19461840]
70. Scheufler C, Sebald W, Hulsmeyer M. Crystal structure of human bone morphogenetic protein-2 at 2.7 A resolution. J Mol Biol. 1999; 287:103–115. [PubMed: 10074410]
71. Cowtan K. Recent developments in classical density modification. Acta Crystallographica Section D. 2010; 66:470–478.
72. Cowtan K. The Buccaneer software for automated model building. 1. Tracing protein chains. Acta Crystallogr D Biol Crystallogr. 2006; 62:1002–1011. [PubMed: 16929101]
73. Emsley P, Cowtan K. Coot: model-building tools for molecular graphics. Acta Crystallogr D Biol Crystallogr. 2004; 60:2126–2132. [PubMed: 15572765]
74. BUSTER, version 2.8.0. v. 2.8.0. Cambridge: 2011.
75. Adams PD, et al. PHENIX: a comprehensive Python-based system for macromolecular structure solution. Acta Crystallographica Section D. 2010; 66:213–221.
76. Davis IW, et al. MolProbity: all-atom contacts and structure validation for proteins and nucleic acids. Nucleic Acids Res. 2007; 35:W375–383. [PubMed: 17452350]
77. Baker NA, Sept D, Joseph S, Holst MJ, McCammon JA. Electrostatics of nanosystems: Application to microtubules and the ribosome. Proceedings of the National Academy of Sciences. 2001; 98:10037–10041.
78. The PyMOL Molecular Graphics System. Version 1.7.2 Schrödinger, LLC.
79. Krissinel E, Henrick K. Inference of macromolecular assemblies from crystalline state. J Mol Biol. 2007; 372:774–797. [PubMed: 17681537]
80. Pernot P, et al. Upgraded ESRF BM29 beamline for SAXS on macromolecules in solution. J Synchrotron Radiat. 2013; 20:660–664. [PubMed: 23765312]
81. Petoukhov MV, et al. New developments in the ATSAS program package for small-angle scattering data analysis. J Appl Crystallogr. 2012; 45:342–350. [PubMed: 25484842]
82. Rambo RP, Tainer JA. Accurate assessment of mass, models and resolution by small-angle scattering. Nature. 2013; 496:477–481. [PubMed: 23619693]
83. Leaver-Fay A, et al. ROSETTA3: an object-oriented software suite for the simulation and design of macromolecules. Methods Enzymol. 2011; 487:545–574. [PubMed: 21187238]
84. Eswar N, et al. Tools for comparative protein structure modeling and analysis. Nucleic Acids Res. 2003; 31:3375–3380. [PubMed: 12824331]
85. Weinkam P, Pons J, Sali A. Structure-based model of allostery predicts coupling between distant sites. Proc Natl Acad Sci U S A. 2012; 109:4875–4880. [PubMed: 22403063]
86. Pelikan M, Hura GL, Hammel M. Structure and flexibility within proteins as identified through small angle X-ray scattering. Gen Physiol Biophys. 2009; 28:174–189. [PubMed: 19592714]
87. Schneidman-Duhovny D, Hammel M, Tainer JA, Sali A. Accurate SAXS profile computation and its assessment by contrast variation experiments. Biophys J. 2013; 105:962–974. [PubMed: 23972848]
88. Guttman M, Weinkam P, Sali A, Lee KK. All-atom ensemble modeling to analyze small-angle x-ray scattering of glycosylated proteins. Structure. 2013; 21:321–331. [PubMed: 23473666]
89. Johnsson B, Löfås S, Lindquist G. Immobilization of proteins to a carboxymethyldextran-modified gold surface for biospecific interaction analysis in surface plasmon resonance sensors. Analytical Biochemistry. 1991; 198:268–277. [PubMed: 1724720]
90. Herrera B, Inman GJ. A rapid and sensitive bioassay for the simultaneous measurement of multiple bone morphogenetic proteins. Identification and quantification of BMP4, BMP6 and BMP9 in bovine and human serum. BMC Cell Biol. 2009; 10:20. [PubMed: 19298647]

91. Korchynskyi O, ten Dijke P. Identification and functional characterization of distinct critically important bone morphogenetic protein-specific response elements in the Id1 promoter. J Biol Chem. 2002; 277:4883–4891. [PubMed: 11729207]
92. Perry GLW. SpPack: spatial point pattern analysis in Excel using Visual Basic for Applications (VBA). Environmental Modelling & Software. 2004; 19:559–569.
93. R Development Core Team. R: A language and environment for statistical computing. R Foundation for Statistical Computing; Vienna, Austria: 2008. ISBN 3-900051-07-0, URL http://www.R-project.org
94. Rossy J, Owen DM, Williamson DJ, Yang Z, Gaus K. Conformational states of the kinase Lck regulate clustering in early T cell signaling. Nat Immunol. 2013; 14:82–89. [PubMed: 23202272]
95. Owen DM, et al. PALM imaging and cluster analysis of protein heterogeneity at the cell surface. J Biophotonics. 2010; 3:446–454. [PubMed: 20148419]
96. Rasband, WS. ImageJ. U. S. National Institutes of Health; Bethesda, Maryland, USA: 2014. http://imagej.nih.gov/ij/
97. Owen DM, Williamson D, Magenau A, Gaus K. Optical techniques for imaging membrane domains in live cells (live-cell palm of protein clustering). Methods Enzymol. 2012; 504:221–235. [PubMed: 22264537]
98. Williamson DJ, et al. Pre-existing clusters of the adaptor Lat do not participate in early T cell signaling events. Nat Immunol. 2011; 12:655–662. [PubMed: 21642986]

Europe PMC Funders Author Manuscripts

Europe PMC Funders Author Manuscripts

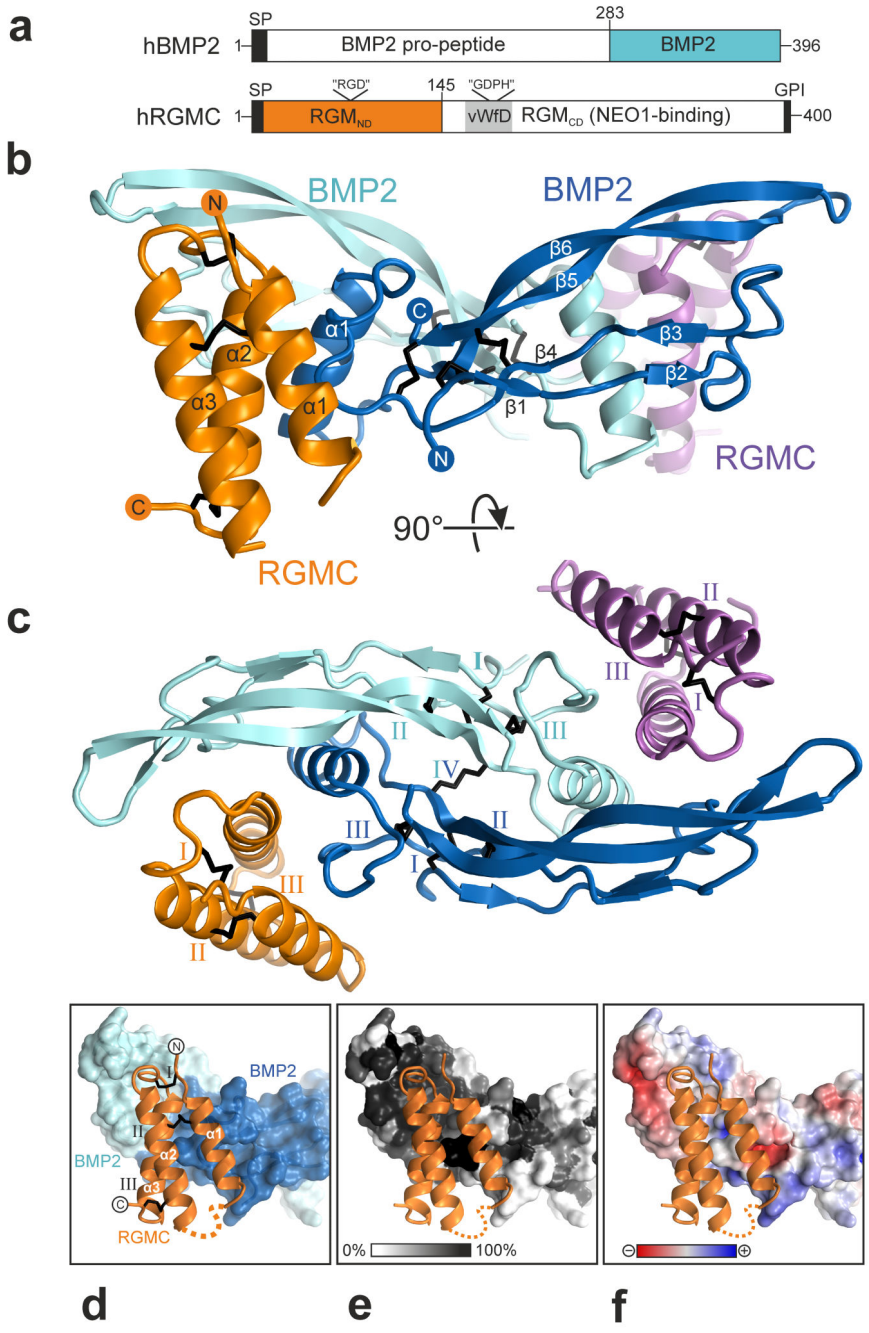

Figure 1. Structure of the BMP2–RGM complex

(a) Schematic of human BMP2 and RGMC. SP = signal peptide, GPI = glycosylphospatidylinositol anchor, vWfD = von Willebrand Factor D-like domain. The potential integrin interaction motif ("RGD") and the autocatalytic cleavage site residues ("GDPH") of RGMC[9] are shown. **(b)** Cartoon representation of the BMP2–RGMC$_{ND}$ complex. BMP2 is shown in blue and cyan, RGMC$_{ND}$ in orange and violet. **(c)** View is rotated 90° around the x-axis compared to (b). Disulfide bonds (black sticks) are depicted with Roman numerals. **(d-f)** Surface representation of the BMP2 "finger" region showing

the RGM binding site. RGMC is in ribbon representation. Disordered regions are shown as dotted lines. Orientation is as in (b). **(d)** The BMP dimer is color-coded as in (b). **(e)** Amino acid residue conservation (from non-conserved, white, to conserved, black) is mapped onto the BMP2 dimer surface based on alignments containing sequences from all available vertebrate BMP2, BMP4, BMP6 and BMP7 family members. **(f)** Electrostatic potential from red ($-8\ k_bT/e_c$) to blue ($8\ k_bT/e_c$) is mapped onto the BMP2 dimer surface.

Europe PMC Funders Author Manuscripts

Europe PMC Funders Author Manuscripts

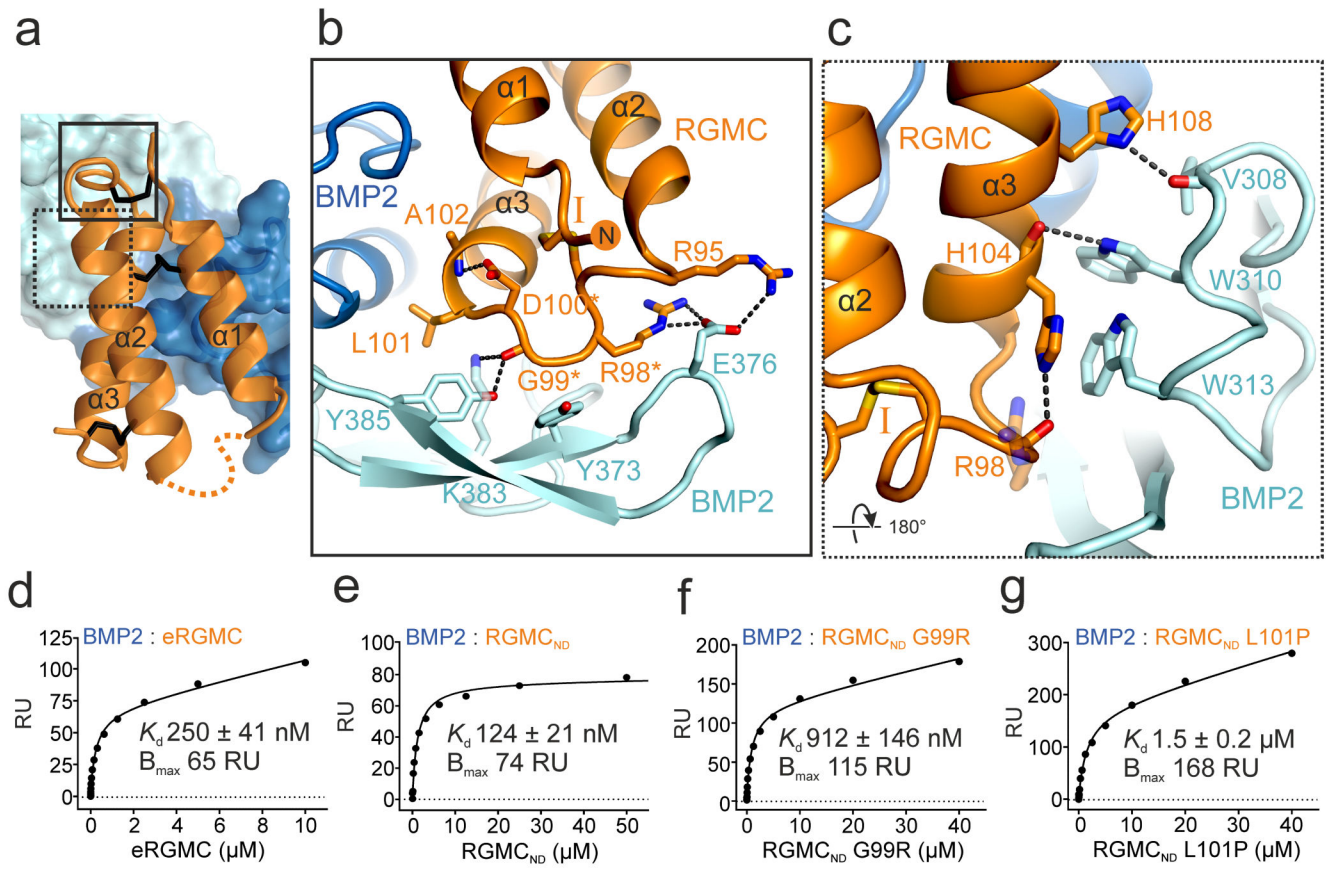

Figure 2. Interaction determinants of the BMP2–RGM complex

(a) Surface representation of the BMP2 dimer showing the RGM binding site. Two regions containing key RGM–BMP interactions are highlighted by boxes. **(b-c)** Close-up view of the BMP2–RGMC interface. Color-coding is as in Fig.1b. Selected interface residues are shown in stick representation. Hydrogen bonds are depicted as dotted lines. **(b)** The "RGD" motif is highlighted by asterisks. **(c)** The π-stacking interaction between RGMC–H104 and BMP2–W313 is shown. **(d-g)** SPR equilibrium-binding. Different concentrations of eRGMC (d), $RGMC_{ND}$ (e) and the JHH-causing mutations $RGMC_{ND}$–G99R (f) and $RGMC_{ND}$–L101P (g) were injected over surfaces coupled with BMP2 (150 RU (d, e), 550 RU (f), 1000 RU (g)). RU: response units. Error range, s.e.m.

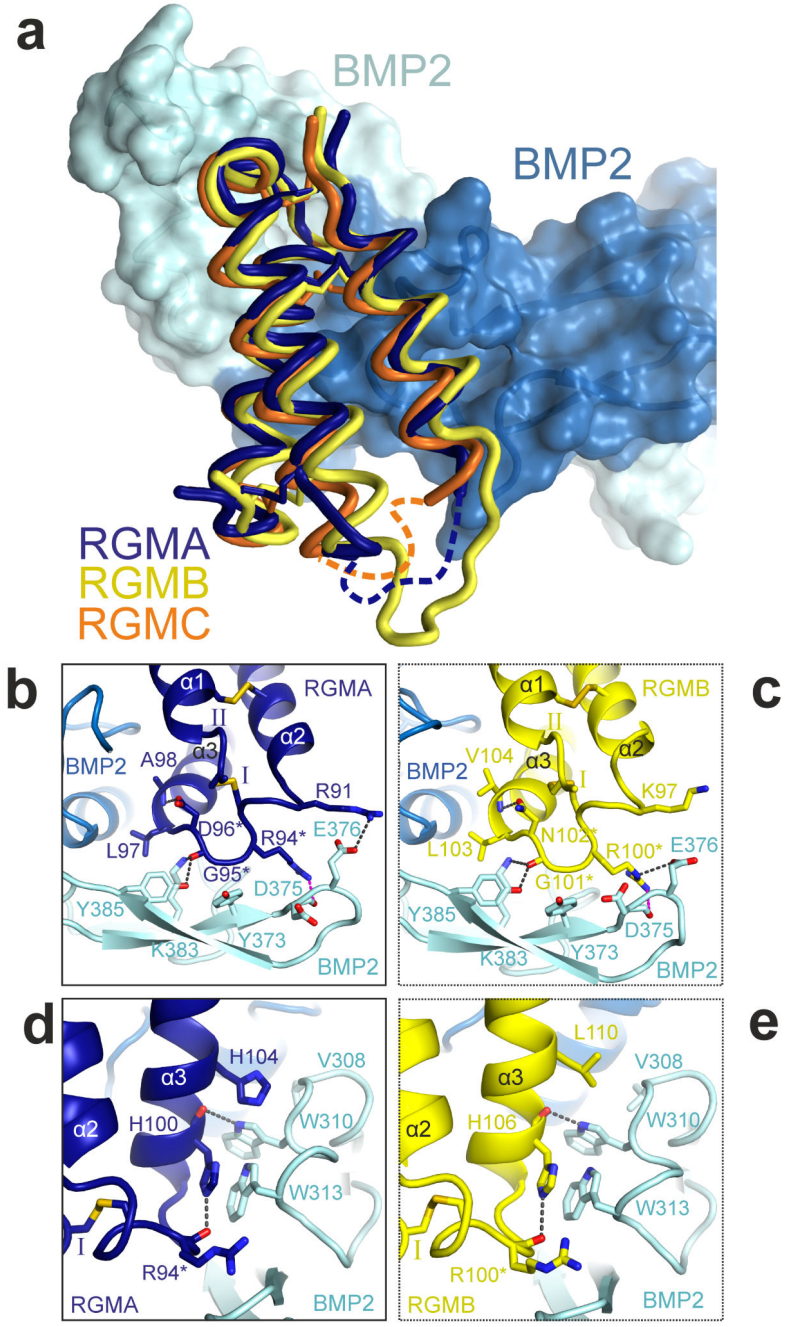

Figure 3. The mode of RGM–BMP2 interactions is conserved in RGMA, RGMB and RGMC

(a) Superposition of BMP2–$RGMA_{ND}$, –$RGMB_{ND}$ and –$RGMC_{ND}$ complex structures with the BMP2 dimer as reference. BMP2 dimer is shown as solvent accessible surface. RGMA (blue), RGMB (yellow) and RGMC (orange) are depicted as ribbons. Orientation is as in Fig. 1d. **(b-e)** Close-up views of the RGM–BMP2 interfaces. Orientation is as in Fig. 2b and c. Labeled residues are shown as sticks. The "RGD" motif is indicated by asterisks in (b-c). Note that the aspartate in the "RGD" motif is replaced with an asparagine in RGMB (c). Both the RGM "RGD" region and the π stacking interactions (mediated via RGM helix α3

and the two BMP2 residues W310 and W313) are conserved in all RGMs. Disulfide bonds are labeled with Roman numerals. Dashed lines indicate hydrogen bonds.

Europe PMC Funders Author Manuscripts

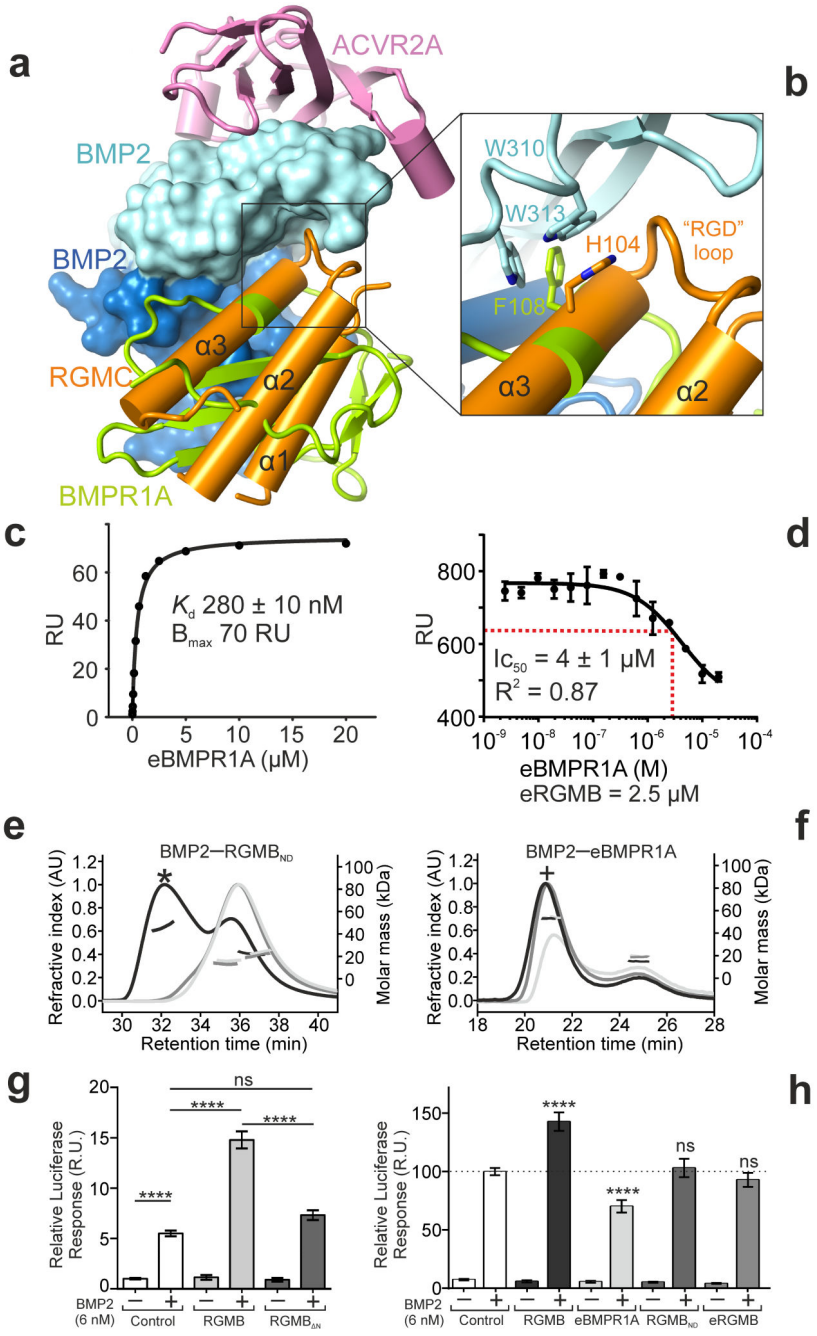

Figure 4. RGMs and BMPR1A share a common binding site on BMP2

(a) $BMP2–RGMC_{ND}$, and BMP2–eBMPR1A–eACVR2A (pdb code 2GOO[39]) complexes are superimposed. BMP2 surface (light and dark blue) and $RGMC_{ND}$ (orange), eBMPR1A (green) and eACVR2A (pink) ribbons are shown. **(b)** Close-up of the BMP2-binding region of RGMC and BMPR1A. **(c)** SPR equilibrium binding experiment of eBMPR1A to BMP2. Error range, s.e.m. **(d)** SPR competition binding experiment between eBMPR1A and eRGMB to BMP2. An IC_{50} value of 4.0±1.0 μM was calculated. R^2=goodness of fit. Error bars, s.e.m. (n=3 technical replicates) **(e–f)** MALS of the $BMP2–RGMB_{ND}$ (e) and the

BMP2–eBMPR1A (f) complexes at pH 7.5 (black), pH 6.5 (dark grey) and pH 5.5 (light grey). Absorbance curves (at 280 nm) are plotted and lines indicate the molecular weights (kDa) of the peaks. The BMP2–$RGMB_{ND}$ complex (46.2±2.7 kDa) is marked by an asterisk and the BMP2–eBMPR1a complex (53.0±0.1/53.2±0.3/54.2±0.5 kDa) is marked by a plus sign. **(g)** SMAD-mediated BMP2 response with co-transfected GPI-anchored RGMB constructs. Three independent experiments. Error bars, s.e.m. (n = 40 except $RGMB_{\Delta N}$ − BMP2 where n=20 cell cultures), **** $P < 0.0001$, ns = 0.0509 by one-way ANOVA with a Tukey multiple comparison test. **(h)** SMAD-mediated BMP2 response with co-transfected eBMPR1A or RGMB ectodomain constructs. Two independent experiments. Error bars, s.e.m. (n = 37, 72, 8, 23, 8, 22, 8, 24, 24, 22 left to right), **** $P < 0.0001$, ns = 0.992 ($RGMB_{ND}$), 0.861 (eRGMB) by one-way ANOVA with Dunnett multiple comparison test.

Europe PMC Funders Author Manuscripts

Europe PMC Funders Author Manuscripts

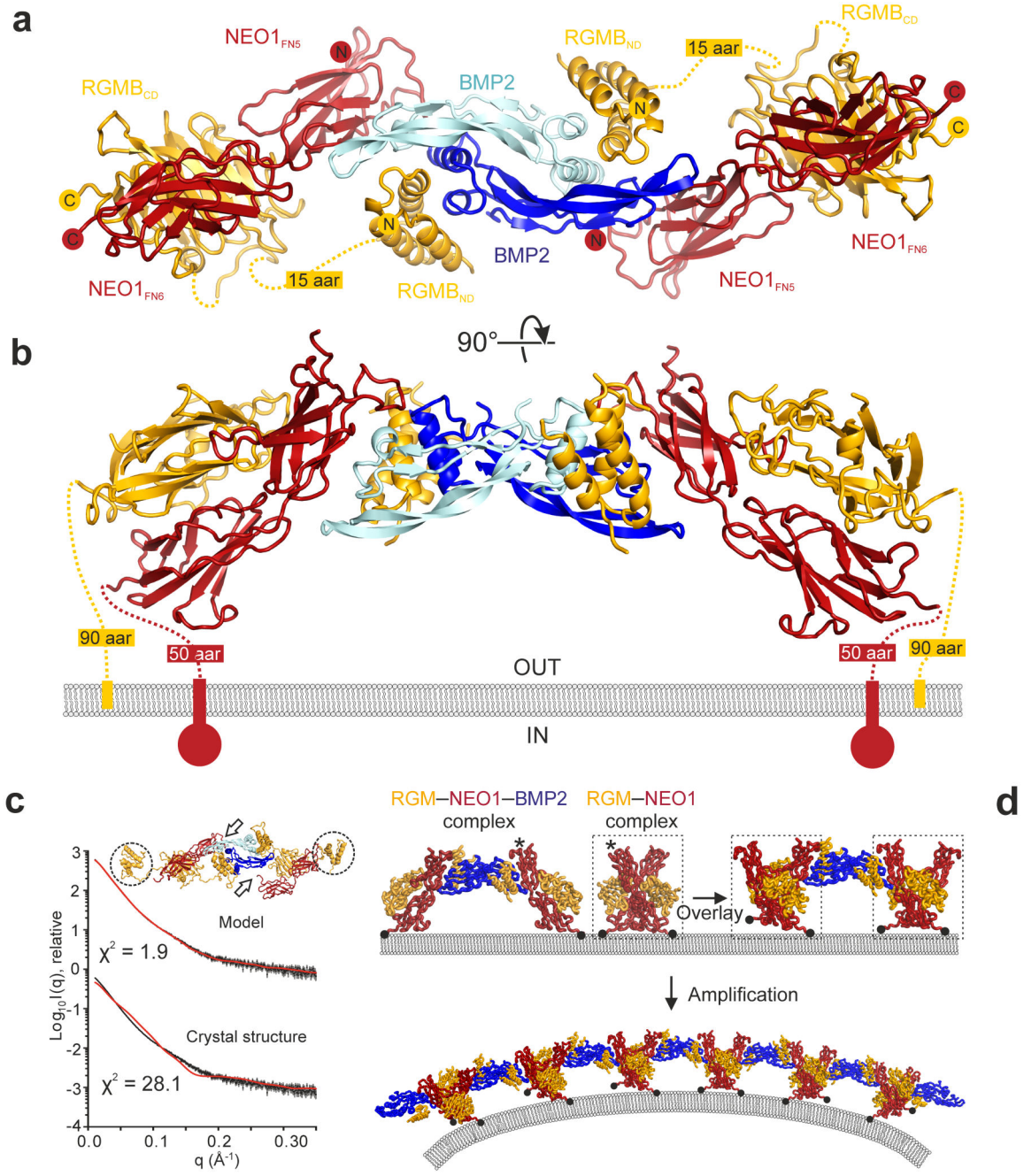

Figure 5. Structure of the ternary BMP2–RGM–NEO1 complex

(a-b) Ribbon representation of the 2:2:2 eRGMB–BMP2–NEO1$_{FN56}$ complex. BMP2 (light and dark blue), RGMB (orange), NEO1 (red). Disordered regions are depicted as dotted lines, with length in number of amino acid residues (aar) indicated. **(c)** SAXS solution structure of the eRGMB–BMP2–NEO1$_{FN56}$ complex. Experimental scattering curves (black) and calculated scattering patterns (red) are shown to a maximal momentum transfer of q = 0.35 Å^{-1}. Bottom curve: ternary complex crystal structure. Top curve: modeled ternary complex ensemble. **(d)** Model of RGM-mediated clustering based on crystal

structure analysis. Superposition of the ternary eRGMB–BMP2–$NEO1_{FN56}$ and the active signal conformation of the RGMB–$NEO1_{FN56}$ complex (pdb 4BQ6[9]) using NEO1 (marked with an asterisk) as template, results in a continuous arrangement in which RGMB bridges the dimers of BMP2 and NEO1, respectively. The C-termini of NEO1 and RGMB are marked by black dots.

Europe PMC Funders Author Manuscripts

Europe PMC Funders Author Manuscripts

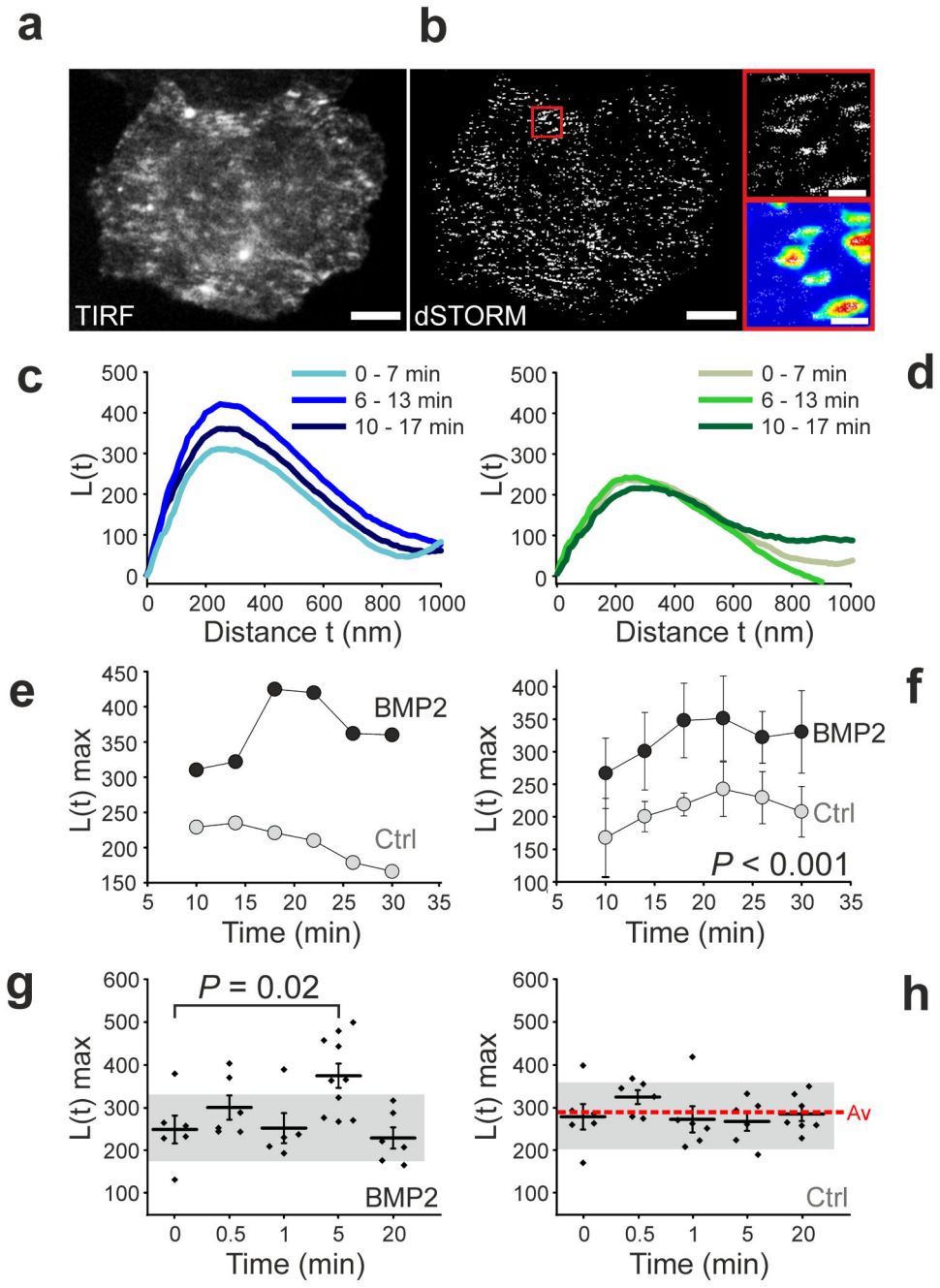

Figure 6. BMP2-mediated clustering of RGM-–NEO1 complexes

(a–b) Live-TIRF (a) and live-TIRF-dSTORM (b) images of a COS7 cell co-expressing NEO1-mVenus and RGMB, treated with BMP2. Scale bars 10 μm. Cluster maps generated from a 5 × 5 μm region of interest (ROI) (red square in (b)) are depicted. Scale bars: 1.5 μm. Bottom right panel of (b): cluster heat map (blue–red, low to high clustering). **(c-d)** Ripley's K-function (L(t)), calculated from a ROI of a single BMP2-treated (c) or control-treated (d) cell. Time-gated window ~ 7 minutes (2000 frames). **(e)** Plot of the maxima of the Ripley's K function (L(t)max) from the experiments shown in (c) and (d) at the indicated time points.

BMP2-treated (black dots, from (c)) or control ("Ctrl", white dots, from (d)) are labeled. **(f)** Mean L(t)max calculated for all analyzed live cells either BMP2-treated (black dots, n = 8 cells) or control ("Ctrl", white dots, n = 6 cells). BMP2 addition at time = 0 min. Error bars, s.d., $P<0.001$ by two-tailed Student's t-test. **(g-h)** Plots of L(t)max of ROIs from different populations of fixed cells treated with either BMP2 (g) and control (h) for the indicated amount of time. Each point is one cell. The horizontal lines represent the mean L(t)max and the error bars are s.e.m. The dotted red line highlights the average L(t)max (255), and the grey square the s.d. (+/−55) for the control. $P = 0.02$ at t = 5 min in the BMP2-treated cells, by two-tailed Student's t-test.

Europe PMC Funders Author Manuscripts

Table 1
Data collection and refinement statistics

	$RGMA_{ND}$–BMP2	$RGMB_{ND}$–BMP2 Form 1	$RGMB_{ND}$–BMP2 Form 2	$RGMC_{ND}$–BMP2	eRGMB–BMP2–$NEO1_{FN56}$
Data collection					
Space group	$P3_221$	$I2_13$	$P3_221$	$P2_12_12_1$	$P4_32_12$
Cell dimensions					
a, *b*, *c* (Å)	83.9, 83.9, 114.8	129.0, 129.0, 129.0	85.0, 85.0, 115.2	69.0, 76.3, 81.7	120.1, 120.1, 204.1
A, *β*, *γ* (°)	90, 90, 90	90, 90, 90	90, 90, 90	90, 90, 90	90, 90, 90
Resolution (Å)	45.00-3.20 (3.42-3.20)[a]	50.00-2.85 (2.93-2.85)	45.00-2.80 (2.80-2.70)	50.00-2.35 (2.43-2.35)	103.50-3.15 (3.23-3.15)
R_{merge}	0.15 (0.74)	0.05 (0.81)	0.10 (0.59)	0.14 (0.79)	0.08 (1.64)
R_{pim}	0.06 (0.29)	0.03 (0.50)	0.04 (0.39)	0.05 (0.71)	0.03 (0.62)
$CC_{1/2}$	0.994 (0.970)	0.998 (0.550)	0.999 (0.934)	0.998 (0.589)	0.999 (0.815)
$I / \sigma I$	9.1 (3.0)	15.1 (1.5)	14.7 (2.7)	11.7 (2.0)	20.2 (1.5)
Completeness (%)	100 (100)	99.4 (98.9)	99.6 (99.4)	99.9 (100.0)	98.6 (96.1)
Redundancy	7.1 (7.3)	4.2 (4.0)	9.6 (9.0)	5.7 (5.1)	8.7 (869)
Refinement					
Resolution (Å)	45.00-3.20	50.00-2.85	45.00-2.80	45.00-2.35	50.00-3.15
No. reflections	8074	8427	12284	18135	26105
R_{work} / R_{free}	0.227/0.264	0.217/0.236	0.233/0.266	0.187/0.238	0.192/0.227
No. atoms					
Protein	2112	1344	2017	2730	4231
Ligand/ion	-	40	22	29	73
Water	-	-	20	85	-
B factors					
Protein	110	110	88	55	134
Ligand/ion	-	180	78	74	171
Water	-	-	88	47	-
r.m.s. deviations					
Bond lengths (Å)	0.010	0.008	0.010	0.010	0.011
Bond angles (°)	1.15	0.95	1.07	1.09	1.540

Each structure was determined from one crystal.

[a] Values in parentheses are for highest-resolution shell.